

ATLAS PUB Note

ATL-PHYS-PUB-2025-037 1st October 2025 Minor revision: 3rd October 2025



Combined effective field theory interpretation of $t\bar{t}$ rapidity and energy asymmetry measurements using $\sqrt{s} = 13$ TeV ATLAS data

The ATLAS Collaboration

Measurements of the rapidity asymmetry in top-quark pair production and the energy asymmetry in the top-quark pair production associated with an energetic jet provide information on effective field theory parameters. A combination of the rapidity asymmetry and energy asymmetry measurements is performed, taking the correlations between the systematic uncertainties and the statistical correlations due to overlapping events into account. Using a combined fit, limits on several Standard Model effective field theory coefficients are set. The combined results resolve directions in the coefficient space which are insensitive in the individual measurements.

Update 3rd October 2025: The caption of the Figure 2 have been corrected, so the colours in the description match ones used in the Figure.

1 Introduction

At the Large Hadron Collider (LHC), the top quark is dominantly produced in top-quark pairs $(t\bar{t})$. At leading order (LO) in quantum chromodynamics (QCD), the $t\bar{t}$ production is symmetric under charge conjugation. However, after including higher-order QCD corrections, a non-zero charge asymmetry arises from interference of amplitudes. This asymmetry has its origin in radiative corrections to $q\bar{q} \to t\bar{t}$ involving either virtual or real gluon emission, and from interference terms of different amplitudes contributing to $qg \to t\bar{t}q$ production. The contributions from gluon fusion remain symmetric to all orders. Due to the charge asymmetry, the top quark (top antiquark) is predominantly produced in the direction of the incoming quark (antiquark) [1–3].

In $t\bar{t}$ production, the charge asymmetry effect can be measured as central-forward rapidity asymmetry (A_Y) [4, 5], which is expressed via the rapidity of the top quark (y_t) and top antiquark $(y_{\bar{t}})$ as follows:

$$A_Y = \frac{N(\Delta|y| > 0) - N(\Delta|y| < 0)}{N(\Delta|y| > 0) + N(\Delta|y| < 0)},\tag{1}$$

where $\Delta |y| = |y_t| - |y_{\bar{t}}|$. The sign of $\Delta |y|$ provides the information about the direction of flight of the top quark. In $q\bar{q}$ annihilation, larger absolute rapidity values are expected from a particle which emerges in the direction of the incoming quark, as this valence quark carries a larger fraction of the proton momentum than the interacting sea antiquark.

The charge asymmetry can also be tested at LO in QCD using the top-quark pair production associated with a hard jet $(t\bar{t}j)$, which contributes to the inclusive $t\bar{t}$ production at NLO in QCD. In $t\bar{t}j$ production, taking into account the relation between the particles' four momenta in the final state, the scattering angles of the top quark and top antiquark with respect to the jet direction are connected to their energies. Therefore, the effect of the charge asymmetry can be studied in terms of the energy asymmetry [6, 7] using the energy difference between the top quark and the top antiquark, $\Delta E = E_t - E_{\bar{t}}$ and the production angle (θ_j) of the jet with the highest transverse momenta defined in the $t\bar{t}j$ rest frame.

The main contribution to the energy asymmetry comes from $gq \to t\bar{t}q$. Here, the final-state-quark jet is boosted in the direction of the initial quark, which affects the rapidity of the $t\bar{t}j$ system in the laboratory frame. Therefore, the optimised cross section, $\sigma^{\rm opt}(\theta_j)$, is defined to optimise statistical sensitivity, combining forward events with positive rapidity of the $t\bar{t}j$ system and backward events with negative rapidity of the $t\bar{t}j$ system:

$$\sigma^{\text{opt}}(\theta_j) = \sigma(\theta_j | y_{t\bar{t}j} > 0) + \sigma(\pi - \theta_j | y_{t\bar{t}j} < 0), \ \theta_j \in [0, \pi].$$
 (2)

Using the optimised cross section, the energy asymmetry (A_E) can be defined as:

$$A_{E}(\theta_{j}) = \frac{\sigma_{E,A}}{\sigma_{E,S}} = \frac{\sigma^{\text{opt}}(\theta_{j}|\Delta E > 0) - \sigma^{\text{opt}}(\theta_{j}|\Delta E < 0)}{\sigma^{\text{opt}}(\theta_{j}|\Delta E > 0) + \sigma^{\text{opt}}(\theta_{j}|\Delta E < 0)},$$
(3)

where $\sigma_{E,S}$ and $\sigma_{E,A}$ denote the charge-symmetric and charge-asymmetric cross-sections. The energy asymmetry increases with transverse momentum of the additional jet [7].

In this note, we present the combination of the ATLAS Run 2 measurements of the differential rapidity asymmetry [8] as a function of the invariant mass and energy asymmetry [9], which are sensitive to a subset of the same Standard Model effective field theory (SMEFT) [10] operators. In the combined fit,

the correlations of the systematic uncertainties are considered, also accounting for the statistical overlap between analyses. The limits on SMEFT operators derived from the combination of the measurements provide a powerful tool for probing physics beyond the Standard Model [7].

2 Input analyses

The rapidity asymmetry was measured inclusively and differentially as a function of the invariant mass $(m^{t\bar{t}})$, transverse momentum $(p_T^{t\bar{t}})$ and longitudinal boost $(\beta_z^{t\bar{t}})$ of the $t\bar{t}$ system, in the single-lepton and dilepton decay channels of $t\bar{t}$ production [8]. In the single-lepton decay channel, the data were divided into resolved and boosted regions, defined by the event topology. In the boosted topology, the jets coming from the hadronic top-quark decay are collimated into a large-radius jet. Fully Bayesian Unfolding (FBU) [11] was performed in order to correct measured spectra for detector effects. Both, the inclusive and the differential measurement of the asymmetry as a function of $m^{t\bar{t}}$ were used to derive limits on SMEFT coefficients.

The energy asymmetry measurement [9] used single-lepton $t\bar{t}$ events with an additional high- p_T jet, which was reconstructed as a large-radius jet. The energy asymmetry was measured in three θ_j bins in a fiducial phase space. The same unfolding technique, FBU, was used to derive the asymmetry values, which were used to extract limits on SMEFT coefficients.

The object definition, event selection criteria and systematic uncertainties for the two measurements are detailed in References [8] and [9].

A statistical overlap between the data used in the rapidity and energy asymmetry measurements is present due to the selection employed in the two analyses. The statistical overlap is evaluated using the so-called bootstrapping technique using the BootstrapGenerator tool [12]. Bootstrap replicas are created by re-weighting data events using generated weights drawn from Poisson distribution with a mean of one. The random seed is determined by using the event identifier, and therefore the same set of Poisson weights is used for the same data event in both analyses. For each event, a set of 1000 replica weights is generated.

The statistical (anti-)correlations between the selected events in the input analyses are taken into account in the combination. The correlations between the events from the A_E measurement and the single-lepton boosted region in the A_Y measurement are estimated to be approximatelly 26%. The (anti-)correlations between the events from the A_E measurement and the single-lepton resolved region in the A_Y measurement varies between 0% and 5%.

3 Combination

A simultaneous extraction of rapidity asymmetry values in five $m^{t\bar{t}}$ bins and energy asymmetry values in three θ_j bins including correlations is performed. These parameters of interest (POIs) and their uncertainties are obtained by minimising a χ^2 likelihood function in the spirit of Reference [13], which includes information from both measurements. Furthermore, limits on the relevant Wilson coefficients are extracted.

The systematic uncertainties from the input analyses are incorporated in the fit (χ^2 likelihood function) as a set of nuisance parameters (NPs). These account for various experimental and theoretical uncertainties affecting both, signal and background modelling. The statistical model for the combination assumes

Gaussian approximations of POIs and NPs. This is fulfilled for all of the NPs, with the exception of the gamma parameters representing the background Monte-Carlo simulation (MC) statistical uncertainties in both measurements. For the gamma parameters, a Gaussian approximation is assumed by transforming the original Poisson distribution to a Gaussian PDF with a mean of zero and an RMS of one for gamma parameters from both measurements.

In the combination procedure, it is necessary to define how the NPs are correlated. The treatment of correlations depends on the source of the systematic uncertainty and the method used for its estimation. In the combination, the NPs related to the $t\bar{t}$ modelling (with the exception of the $t\bar{t}$ Var3c parameter) are treated as uncorrelated as it is not obvious that the constraints from the rapidity asymmetry can be safely propagated to the energy asymmetry. For the background processes, the NPs related to the single top (tW) diagram subtraction versus diagram removal uncertainty, the single top (tW) parton shower uncertainty in the boosted region, and the W+jets μ_R and μ_F scale variations in the boosted region are considered as fully correlated. Since the input analyses use different definitions for the small-R jets, the NPs related to the jet energy resolutions are kept uncorrelated as there is no one-to-one correspondence between the two sets of NPs. However, as the same methods were used to obtain the jet energy scale (JES) variations in both analyses, the NPs related to JES are treated as fully correlated. Among the other NPs, those related to common sources of systematic uncertainties are considered fully correlated as well. Specifically, the NPs related to the reconstruction of the missing transverse momentum, the re-weighting of the MC pile-up distribution, luminosity measurements, jet vertex tagger requirements and parton distribution functions used for $t\bar{t}$ modelling. All other NPs are treated as fully uncorrelated.

The results of the rapidity asymmetry A_Y and energy asymmetry A_E obtained from the combination assuming the correlations among the NPs described above are summarised in Table 1 and Table 2, respectively, and in Figure 1. The results of the combination are compared to the results of the input analyses. The uncertainties of the asymmetries obtained by the combination assuming correlations are relatively improved by about 1%. Although the impact of the combination is small, the combinations resolves the blind directions in the parameter space (see Section 4). In addition, the results of the combination assuming no correlations among the NPs of the input analyses are presented in Tables 1 and 2. As can be seen, the choice of the assigned correlations does not have a significant impact on the analysis. The rapidity asymmetry values are compared to the SM predictions [14] calculated at NNLO in QCD and NLO in EW theory in Figure 1.

Additionally, the 20 most important NPs from each analysis have been used to test several different correlation scenarios. These NPs are mostly related to the modelling of $t\bar{t}$ and single top productions. In each correlation scenario, a single NP has been considered either to be uncorrelated or fully correlated among the two analysis and in the case of NPs that were decorrelated in the input analysis (e.g. $t\bar{t}$ FSR) per component correlations have been tested. The considered alternative scenarios have been found to have no significant impact on the uncertainties of the combined result. The highest relative difference in the uncertainty (of about 4%) was found when the $t\bar{t}$ FSR modelling NP related to the 4th $m^{t\bar{t}}$ bin for the boosted topology of the rapidity asymmetry measurement was fully correlated to the $t\bar{t}$ FSR NP from the energy asymmetry measurement.

¹ In the rapidity asymmetry measurement, some of the $t\bar{t}$ and single top modelling NPs were decorrelated by $m^{t\bar{t}}$ differential bins and by event topology (resolved/boosted), while there is only a single corresponding NP in the energy asymmetry measurement.

Table 1: The differential rapidity asymmetries, A_Y , as a function of the invariant mass of the reconstructed top-quark pair $m^{t\bar{t}}$. The results of the combination are obtained assuming (no) correlations with the A_E nuisance parameters. The relative uncertainty difference of the combination assuming correlations with respect to the original measurement [8] is shown in the last row.

	$m^{tar{t}}$ [GeV]				
$\overline{A_Y}$	[0, 500]	[500, 750]	[750, 1000]	[1000, 1500]	> 1500
Reference [8]	0.0059 ± 0.0036	0.0055 ± 0.0023	0.0102 ± 0.0055	0.0246 ± 0.0087	0.0014 ± 0.0288
Combination (no corr.)	0.0060 ± 0.0035	0.0055 ± 0.0023	0.0102 ± 0.0055	0.0246 ± 0.0085	0.0015 ± 0.0286
Combination (corr.)	0.0059 ± 0.0035	0.0055 ± 0.0023	0.0102 ± 0.0055	0.0247 ± 0.0085	0.0014 ± 0.0286
$\frac{(\sigma_{\rm corr} - \sigma_{\rm orig})/\sigma_{\rm orig}}{}$	−1.2%	−1.0%	-0.8%	-1.5%	-0.7%

Table 2: The differential energy asymmetries, A_E , as a function of the production angle of the hard jet in $t\bar{t}j$ events, θ_j . The results of combination are obtained assuming (no) correlations with the A_Y nuisance parameters. The relative uncertainty difference of the combination assuming correlations with respect to the original measurement [9] is shown in the last row.

		$ heta_j$	
A_E	$[0, \pi/4]$	$[\pi/4, 3\pi/4]$	$[3\pi/4,\pi]$
Reference [9]	-0.032 ± 0.021	-0.043 ± 0.020	-0.013 ± 0.018
Combination (no corr.)	-0.032 ± 0.016	-0.043 ± 0.020	-0.013 ± 0.018
Combination (corr.)	-0.032 ± 0.021	-0.042 ± 0.020	-0.010 ± 0.017
$\frac{(\sigma_{\rm corr} - \sigma_{\rm orig})/\sigma_{\rm orig}}{(\sigma_{\rm corr} - \sigma_{\rm orig})/\sigma_{\rm orig}}$	-0.9%	-0.8%	-1.1%

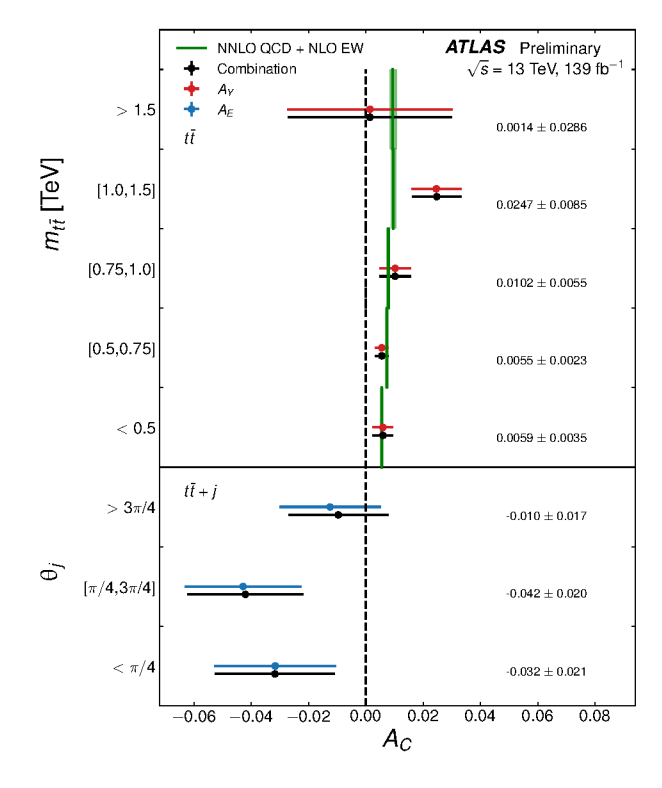


Figure 1: Comparison of the differential rapidity and energy asymmetries obtained from the combination and from the ATLAS results [8, 9]. The SM predictions of the rapidity asymmetry calculated at NNLO in QCD and NLO in EW theory are shown as a green band.

4 SMEFT interpretation

The sensitivity of the charge asymmetry to new physics above a scale Λ is investigated in the framework of SMEFT. To this end, the SM Lagrangian \mathcal{L}_{SM} is extended by a series of local operators O_k ,

$$\mathcal{L}_{\text{SMEFT}} = \mathcal{L}_{\text{SM}} + \sum_{k} \frac{C_k}{\Lambda^2} O_k + \dots$$
 (4)

The sum runs over all SM gauge-invariant operators of mass dimension six and the ellipsis indicates higher-dimensional operators in the SMEFT expansion. The analysis also assumes CP invariance, which implies that all Wilson coefficients C_k are real. Setting all the Wilson coefficients to zero corresponds to the SM. The cut-off scale of this effective theory is set to $\Lambda = 1$ TeV.

To demonstrate the sensitivity of the combined results of the charge asymmetry measurements to the chirality and colour charges of quark fields, the focus of this numerical analysis is on six selected four-quark operators in the Warsaw basis [15, 16]:

$$O_{Qq}^{1,1} = (\bar{Q}_{L}\gamma_{\mu}Q_{L})(\bar{q}_{L}\gamma^{\mu}q_{L}) \qquad O_{Qq}^{1,8} = (\bar{Q}_{L}\gamma_{\mu}T^{A}Q_{L})(\bar{q}_{L}\gamma^{\mu}T^{A}q_{L})$$

$$O_{tq}^{1} = (\bar{q}_{L}\gamma_{\mu}q_{L})(\bar{t}_{R}\gamma^{\mu}t_{R}) \qquad O_{tq}^{8} = (\bar{q}_{L}\gamma_{\mu}T^{A}q_{L})(\bar{t}_{R}\gamma^{\mu}T^{A}t_{R})$$

$$O_{tu}^{1} = (\bar{t}_{R}\gamma_{\mu}t_{R})(\bar{u}_{R}\gamma^{\mu}u_{R}) \qquad O_{tu}^{8} = (\bar{t}_{R}\gamma_{\mu}T^{A}t_{R})(\bar{u}_{R}\gamma^{\mu}T^{A}u_{R}) . \qquad (5)$$

Left-handed quark doublets of the first two generations and the third generation are denoted by

$$q_{L} = (u_{L}, d_{L})^{T}, (c_{L}, s_{L})^{T}, \qquad Q_{L} = (t_{L}, b_{L})^{T},$$

reflecting an assumed flavour symmetry among couplings of the first and second quark generations. Also, $T^A \equiv \lambda^A/2$, where λ^A are Gell-Mann matrices. The six operators defined in Equation 5 feature different chiral structures (LL, RR, LR) and colour structures (singlet (1) and octet (8)), thus covering the relevant properties that can be tested with the charge asymmetry. Operators with right-handed down-type quarks d_R would affect the energy asymmetry very similarly to those with up-type quarks and are therefore not included in this analysis. Up- and down-quark operators can be resolved for instance with $t\bar{t}Z$ or $t\bar{t}W$ observables, which are sensitive to the weak isospin of the quarks [17].

The Wilson coefficients in the effective Lagrangian in Equation 4 parameterise possible effects of virtual new heavy particles in the cross section σ and in asymmetry observables A according to

$$\sigma = \sigma_{\mathcal{S}}^{\mathcal{SM}} + \sum_{k} C_k \sigma_{\mathcal{S}}^k + \sum_{k \leq l} C_k C_l \sigma_{\mathcal{S}}^{kl}, \qquad A = \frac{\sigma_{\mathcal{A}}}{\sigma_{\mathcal{S}}} = \frac{\sigma_{\mathcal{A}}^{\mathcal{SM}} + \sum_{k} C_k \sigma_{\mathcal{A}}^k + \sum_{k \leq l} C_k C_l \sigma_{\mathcal{A}}^{kl}}{\sigma_{\mathcal{S}}^{\mathcal{SM}} + \sum_{k} C_k \sigma_{\mathcal{S}}^k + \sum_{k \leq l} C_k C_l \sigma_{\mathcal{S}}^{kl}}.$$
(6)

The cross sections $\sigma_{S,A}^{SM}$ denote the SM contributions, while $\sigma_{S,A}^k$ and $\sigma_{S,A}^{kl}$ correspond to the interference of a SMEFT amplitude with the SM amplitude at $O(\Lambda^{-2})$ and the pure SMEFT amplitudes at $O(\Lambda^{-4})$, respectively. The charge-symmetric σ_S and charge-asymmetric σ_A cross-sections are defined in Equation 3 for the energy asymmetry. Similarly, we can define them for the rapidity asymmetry as follows:

$$\sigma_{Y,S} = \sigma(\Delta|y| > 0) + \sigma(\Delta|y| < 0),$$

$$\sigma_{Y,A} = \sigma(\Delta|y| > 0) - \sigma(\Delta|y| < 0).$$
(7)

The SM prediction for the energy asymmetry at the particle level was obtained from simulation generated with MadGraph5_aMC@NLO 2.7 [18] interfaced to Pythia 8.2 [19] at NLO in $t\bar{t}j$ production, while

the SM-EFT interference and EFT-EFT contributions were generated at LO using the SMEFTATNLO package [20] (see Reference [9] for further details). The SM prediction for the rapidity asymmetry was calculated at NNLO in $t\bar{t}$ production including electroweak corrections [14], while the operator contributions were calculated at NLO using the SMEFTATNLO package.

This analysis considers MC statistical and scale uncertainties on the SMEFT prediction. In total, there are ten nuisance parameters. There is one nuisance parameter for each bin of the predicted asymmetry A representing the MC statistical uncertainty and two nuisance parameters for scale uncertainties on the SMEFT prediction. Scale uncertainties are taken into account by varying the renormalisation scale μ_R and the factorisation scale μ_F independently up and down by a factor of two. The scales are varied coherently for the SM and EFT contributions.

The limits on the Wilson coefficients are extracted using a profile likelihood fit. The one-dimensional 95% and 68% confidence level limits are shown in Figure 2 and Tables 3 and 4 for the rapidity and energy asymmetry measurements as well as their combination. The quadratic parameterisation that retains the dimension-six-squared terms proportional to Λ^{-4} as well as the Λ^{-2} terms is considered as the quadratic terms have a non-negligible impact on the obtained intervals (see References [8, 9]). A care should be taken to ensure dimension-8 contributions of the same order are negligible when re-interpreting these bounds. In case of non-negligible impact of quadratic terms, violations of Wilks' theorem [21] could be relevant, but their impact has not been assessed quantitatively. Considering MC statistical and scale uncertainties increase the size of confidence intervals by about 5% to 30%.

Table 3: Comparison of the bounds on individual Wilson coefficients C (TeV/ Λ)² from one-parameter quadratic fits obtained from the individual rapidity asymmetry A_Y and energy asymmetry A_E analyses and from their combination. Limits for 68% confidence level are shown.

$C (\text{TeV}/\Lambda)^2$	68% confidence level				
$C(1eV/\Lambda)^2$	A_Y	A_E	combination		
$C_{Oq}^{1,1}$	[-0.52, -0.28]	[-0.38, 0.44]	$[-0.50, -0.26] \cup [0.21, 0.23]$		
$C_{tq}^{Qq} \ C_{tq}^{1,8} \ C_{tq}^{1} \ C_{tq}^{8} \ C_{tu}^{1} \ C_{tu}^{8} \ C_{tu}^{8}$	[0.04, 0.40]	[-0.85, 1.17]	[0.06, 0.45]		
$C_{tq}^{\widetilde{1}^{-1}}$	[-0.09, 0.15]	[-0.42, 0.51]	[-0.08, 0.16]		
C_{tq}^{8}	[-0.34, 0.33]	[-1.41, 0.84]	[-0.29, 0.37]		
C_{tu}^{1}	[-0.67, -0.39]	[-0.46, 0.52]	[-0.64, -0.37]		
C_{tu}^8	[0.14, 0.66]	[-0.96, 0.92]	[0.19, 0.71]		

The limits on the Wilson coefficients for individual rapidity and energy asymmetry measurements are re-derived using a common approach to estimate theoretical uncertainties. In the rapidity asymmetry measurement [8], the theoretical uncertainties related to scales variations and Monte Carlo statistics were considered only for the SM prediction. In this note, these uncertainties are considered also for SM–EFT and EFT–EFT terms. In the energy asymmetry measurement [9], the scale uncertainties for the SM and SMEFT were estimated from the envelope of nine different settings for the renormalisation and factorisation scales. In this note, only up and down variations are considered. The changes in the estimation of the theoretical uncertainties results in some differences compared to the results of the original measurements.

For all of the considered Wilson coefficients, the limits obtained by the combination do not improve significantly on the re-derived limits for the individual rapidity asymmetry measurement. For the cases,

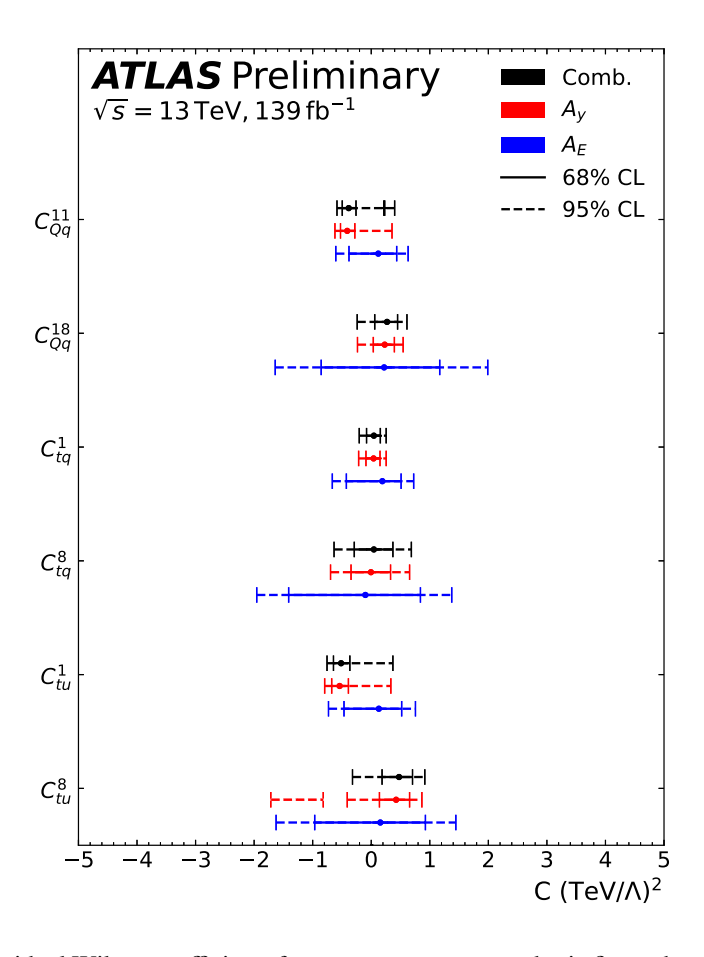


Figure 2: Bounds on individual Wilson coefficients from one-parameter quadratic fits to the energy (blue) and rapidity (red) asymmetries as well as their combination (black), setting all other operator coefficients to zero. The bounds on C (TeV/ Λ)² are reported at the 68% confidence level (solid) and 95% confidence level (dashed). For the $C_{Qq}^{1,1}$ coefficient, the thick black vertical bar represents interval of [0.21,0.23] from the combination.

Table 4: Comparison of the bounds on individual Wilson coefficients C (TeV/ Λ)² from one-parameter quadratic fits obtained from the individual rapidity asymmetry A_Y and energy asymmetry A_E analyses and from their combination. Limits for 95% confidence level are shown.

$C (\text{TeV}/\Lambda)^2$	95% confidence level				
C (TeV/A)	A_Y	A_E	combination		
$C_{Oq}^{1,1}$	[-0.62, 0.36]	[-0.60, 0.63]	[-0.58, 0.40]		
$C_{Qq}^{Qq} \ C_{1,8}^{1,8} \ C_{Qq}^{0q} \ C_{tq}^{1} \ C_{tu}^{8} \ C_{tu}^{1} \ C_{tu}^{8} \ C_{tu}^{8}$	[-0.24, 0.54]	[-1.64, 1.99]	[-0.24, 0.61]		
$C_{tq}^{\widetilde{1}^{-1}}$	[-0.21, 0.25]	[-0.67, 0.73]	[-0.21, 0.25]		
C_{tq}^{8}	[-0.70, 0.66]	[-1.96, 1.38]	[-0.63, 0.69]		
C_{tu}^{1}	[-0.79, 0.33]	[-0.73, 0.75]	[-0.75, 0.37]		
C_{tu}^8	$[-1.71, -0.82] \cup [-0.41, 0.87]$	[-1.62, 1.45]	[-0.32, 0.92]		

where the confidence intervals in the combination are larger than the individual ones, this is caused by the approximations assumed in the combination and by numerical precision. In Figure 2, some differences can be seen for 68% confidence level (CL) limits for $C_{Qq}^{1,1}$ and for 95% CL limits for C_{tu}^8 . The χ^2 fits for $C_{Qq}^{1,1}$ and C_{tu}^8 are compared in Figure 3 and Figure 4, respectively. In both cases, the differences come from effects related to double-minima. For the $C_{Qq}^{1,1}$, the second minimum is below the threshold of the 68% confidence interval, while for C_{tu}^8 the second minimum is above the threshold of the 95% confidence interval.

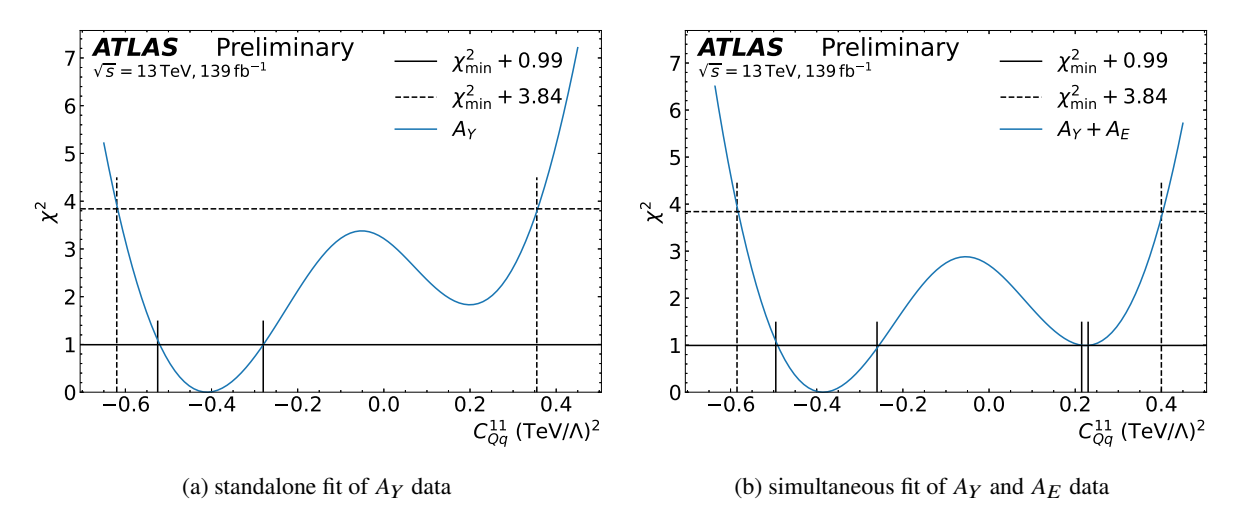


Figure 3: Comparison of χ^2 functions of $C_{Qq}^{1,1}$ fits using only rapidity asymmetry A_Y data (a) and simultaneous fit of rapidity and energy asymmetry data (b). Dashed lines show 95% confidence level limits, solid lines 68% confidence level limits. In the case (b), the second minimum of χ^2 function moved below the threshold for 68% confidence interval

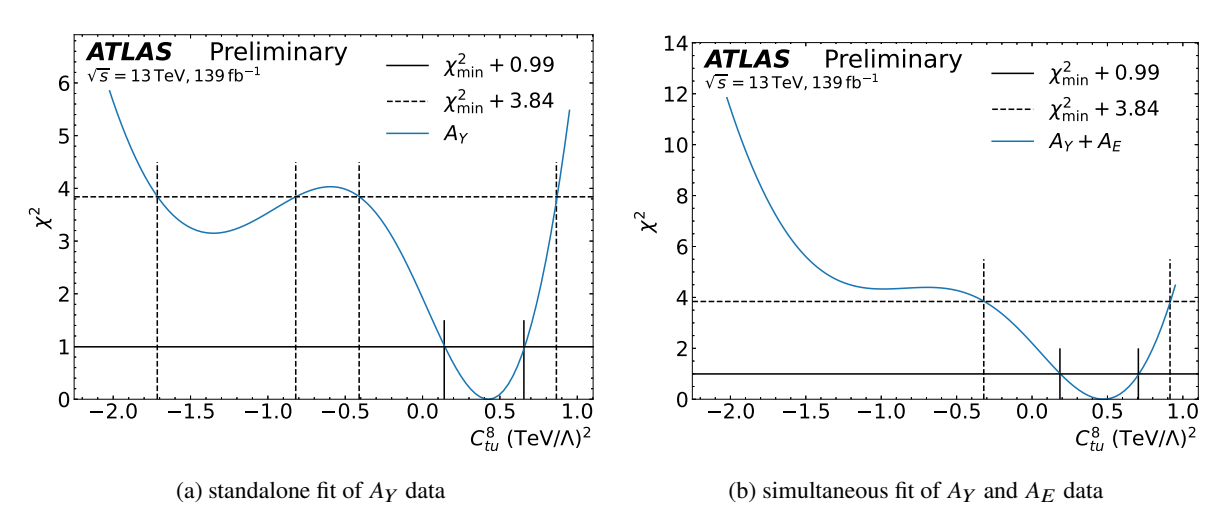


Figure 4: Comparison of χ^2 functions of C_{tu}^8 fits using only rapidity asymmetry A_Y data (a) and simultaneous fit of rapidity and energy asymmetry data (b). Dashed lines show 95% confidence level limits, solid lines 68% confidence level limits. In the case (b), the second minimum of χ^2 function moved above the threshold of 95% confidence interval.

Figure 5 shows the two-dimensional bounds obtained from the individual rapidity and energy asymmetry measurements as well as their combination. Due to the extra jet in $t\bar{t}j$ production, the QCD structure of the energy asymmetry is not the same as for the charge asymmetry in $t\bar{t}$ production, so the two asymmetries probe different directions in chiral and colour space. For colour-singlet operators with different quark chiralities (top row), the two asymmetries probe similar areas in the parameter space. For colour-octet operators with the same chirality scenarios (middle row), however, the shapes of the bounds are very different. In particular, the charge asymmetry leaves a blind direction in the $(C_{Qq}^{1.8}, C_{tq}^8)$ plane (left panel), which is broken by the energy asymmetry due to operator interference with the QCD amplitude. The bottom row shows colour-singlet versus colour-octet operators with the same quark chiralities. Here, the different shapes of the bounds are due to the different colour-singlet and colour-octet contributions to $t\bar{t}$ and $t\bar{t}j$ production, which is probed with high sensitivity by the asymmetries. The EFT contributions include dimension-six-squared terms proportional to Λ^{-4} for both the charge asymmetry and energy asymmetry. A comparison for C_{tu}^1 versus C_{tu}^8 is not included, because the different sensitivity to colour-singlet and colour-octet operators has already been illustrated with C_{tq}^1 versus C_{tq}^8 , and the difference between L and R light quarks has been illustrated with $C_{tq}^{1,1}$ versus C_{tu}^8 .

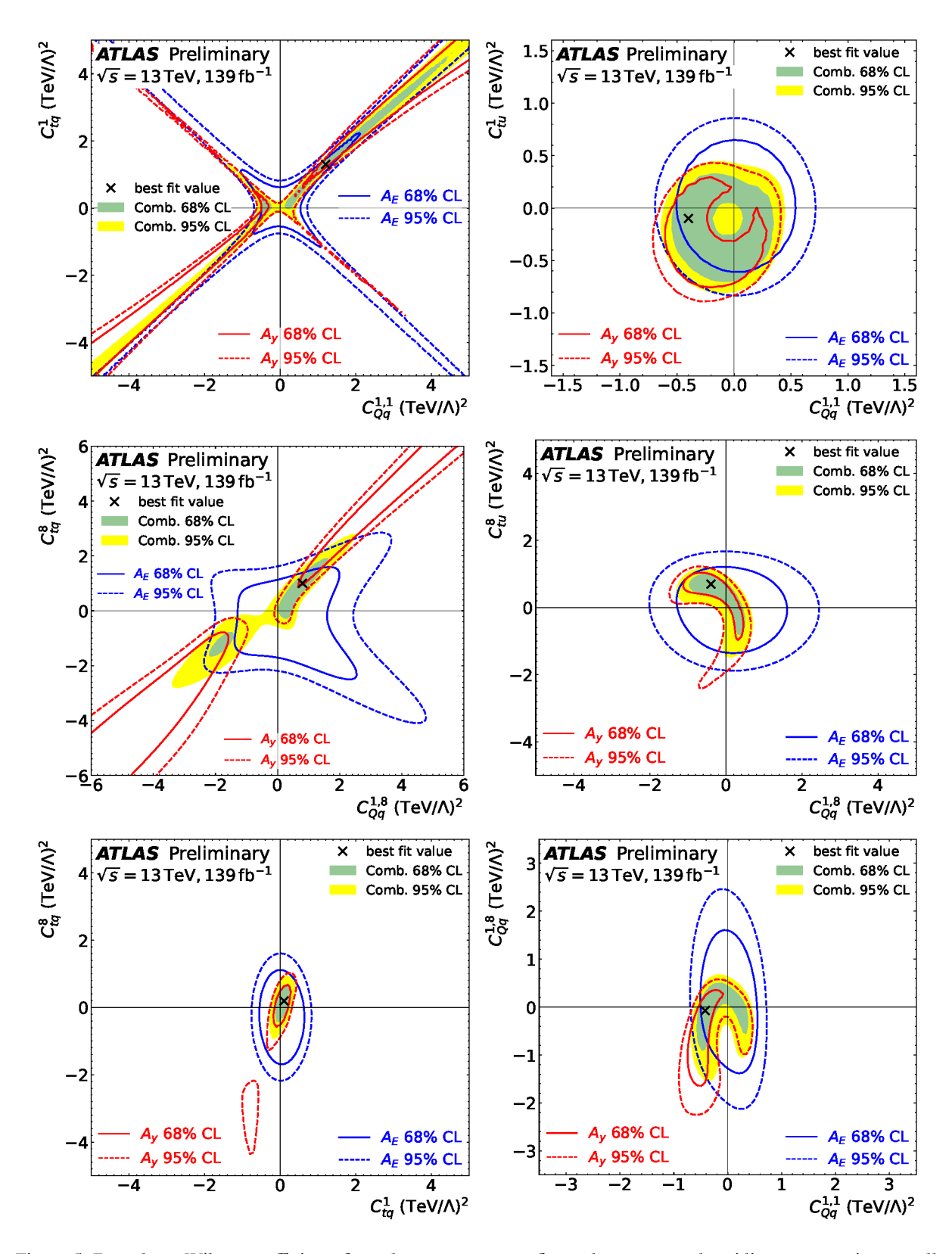


Figure 5: Bounds on Wilson coefficients from the two-parameter fits to the energy and rapidity asymmetries as well as their combination, setting all other operator coefficients to zero. The inner green and outer yellow areas show the 68% and 95% CL areas obtained from the combination. Solid and dashed contours show the 68% and 95% confidence bounds of the energy (blue) and rapidity (red) asymmetries, respectively. The black cross denotes the minimum of the χ^2 fit.

Conclusion

The combination of differential measurements of the rapidity and energy asymmetries in top-quark pair topologies was performed using a simultaneous fit taking into account statistical correlations and correlations between the systematic uncertainties. The results are used to extract limits on the Wilson coefficients of the Standard Model effective field theory, using a common treatment of uncertainties on the theoretical predictions used in this interpretation. While the combination brings little improvement for constraints on single Wilson coefficients, for the colour-octet operators, the combination set limits in the $(C_{Qq}^{1,8}, C_{tq}^{8})$ plane, resolving the blind directions in the standalone rapidity asymmetry measurement.

Appendix

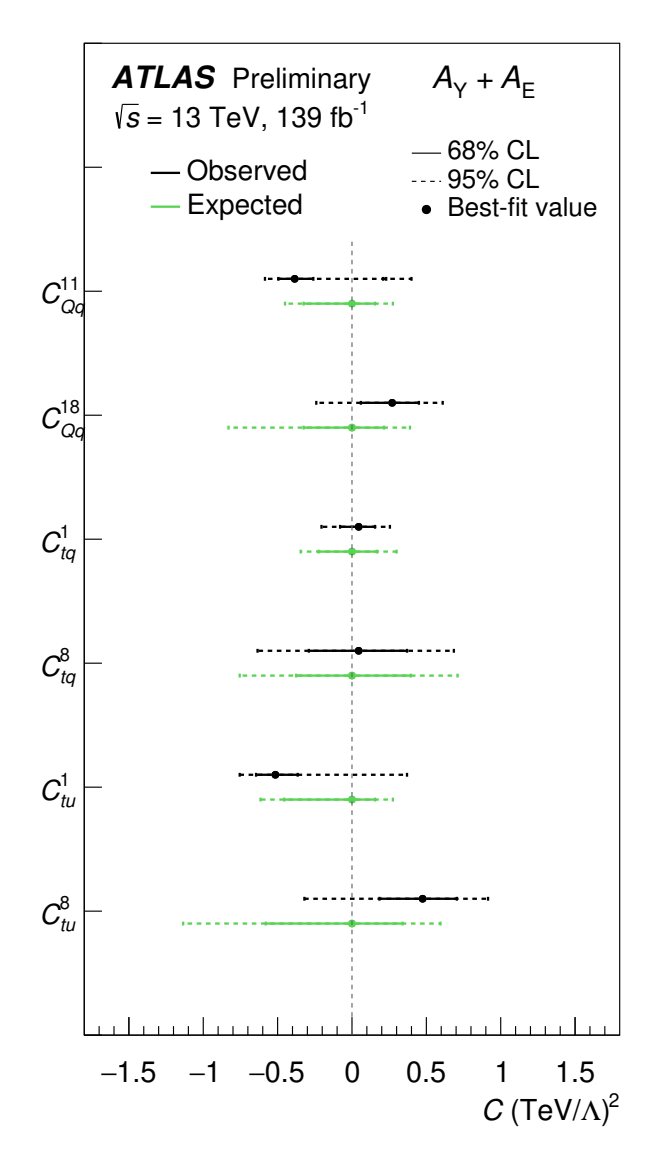


Figure 6: Comparison of observed (black) and expected (green) bounds on individual Wilson coefficients from one-parameter quadratic fits, setting all other operator coefficients to zero, for the combination of the rapidity and energy asymmetry measurements. The bounds on C (TeV/ Λ)² are reported at the 68% confidence level (solid) and 95% confidence level (dashed). For the $C_{Qq}^{1,1}$ coefficient, the observed limits consist of two intervals, having a second minimum of the χ^2 distribution in the interval of [0.21,0.23].

References

[1] J. H. Kühn and G. Rodrigo, *Charge asymmetry of heavy quarks at hadron colliders*, Phys. Rev. D **59** (1999) 054017, arXiv: hep-ph/9807420 (cit. on p. 2).

- [2] J. H. Kühn and G. Rodrigo, *Charge asymmetries of top quarks at hadron colliders revisited*, JHEP **01** (2012) 063, arXiv: 1109.6830 [hep-ph] (cit. on p. 2).
- [3] J. A. Aguilar-Saavedra, D. Amidei, A. Juste and M. Pérez-Victoria, *Asymmetries in top quark pair production at hadron colliders*, Rev. Mod. Phys. **87** (2015) 421, arXiv: 1406.1798 [hep-ph] (cit. on p. 2).
- [4] R. Diener, S. Godfrey and T. A. W. Martin,

 Using final state pseudorapidities to improve s-channel resonance observables at the LHC,

 Phys. Rev. D 80 (2009) 075014 (cit. on p. 2).
- [5] S. Jung, A. Pierce and J. D. Wells, *Top quark asymmetry from a non-Abelian horizontal symmetry*, Phys. Rev. D **83** (2011) 114039 (cit. on p. 2).
- [6] S. Berge and S. Westhoff,

 Top-quark charge asymmetry goes forward: two new observables for hadron colliders,

 JHEP 07 (2013) 179, arXiv: 1305.3272 [hep-ph] (cit. on p. 2).
- [7] A. Basan, P. Berta, L. Masetti, E. Vryonidou and S. Westhoff, *Measuring the top energy asymmetry at the LHC: QCD and SMEFT interpretations*, JHEP **03** (2020) 184, arXiv: 2001.07225 [hep-ph] (cit. on pp. 2, 3).
- [8] ATLAS Collaboration, Evidence for the charge asymmetry in $pp \to t\bar{t}$ production at $\sqrt{s} = 13$ TeV with the ATLAS detector, JHEP **08** (2023) 077, arXiv: 2208.12095 [hep-ex] (cit. on pp. 2, 3, 5, 7).
- [9] ATLAS Collaboration, *Measurement of the energy asymmetry in tīj production at* 13 *TeV with the ATLAS experiment and interpretation in the SMEFT framework*, Eur. Phys. J. C **82** (2022) 374, arXiv: 2110.05453 [hep-ex] (cit. on pp. 2, 3, 5, 7).
- [10] W. Buchmüller and D. Wyler, Effective Lagrangian analysis of new interactions and flavour conservation, Nucl. Phys. B **268** (1986) 621, ISSN: 0550-3213 (cit. on p. 2).
- [11] G. Choudalakis, *Fully Bayesian Unfolding*, (2012), arXiv: 1201.4612 [hep-ex] (cit. on p. 3).
- [12] ATLAS Collaboration,

 Evaluating statistical uncertainties and correlations using the bootstrap method,

 ATL-PHYS-PUB-2021-011, 2021, URL: https://cds.cern.ch/record/2759945 (cit. on p. 3).
- [13] J. Kieseler, A method and tool for combining differential or inclusive measurements obtained with simultaneously constrained uncertainties, Eur. Phys. J. C 77 (2017) 792, arXiv: 1706.01681 [physics.data-an] (cit. on p. 3).
- [14] M. Czakon et al.,

 Top-quark charge asymmetry at the LHC and Tevatron through NNLO QCD and NLO EW,
 Phys. Rev. D 98 (2018) 014003, arXiv: 1711.03945 [hep-ph] (cit. on pp. 4, 7).
- [15] B. Grzadkowski, M. Iskrzynski, M. Misiak and J. Rosiek, Dimension-six terms in the Standard Model Lagrangian, JHEP 10 (2010) 085, arXiv: 1008.4884 [hep-ph] (cit. on p. 6).
- [16] D. Barducci et al.,

 Interpreting top-quark LHC measurements in the Standard-Model Effective Field Theory,

 (2018), ed. by J. A. Aguilar-Saavedra et al., arXiv: 1802.07237 [hep-ph] (cit. on p. 6).

- [17] I. Brivio et al., *O new physics, where art thou? A global search in the top sector*, JHEP **02** (2020) 131, arXiv: 1910.03606 [hep-ph] (cit. on p. 6).
- [18] J. Alwall et al., *The automated computation of tree-level and next-to-leading order differential cross sections, and their matching to parton shower simulations*, JHEP **07** (2014) 079, arXiv: 1405.0301 [hep-ph] (cit. on p. 6).
- [19] T. Sjöstrand et al., *An introduction to PYTHIA* 8.2, Comput. Phys. Commun. **191** (2015) 159, arXiv: 1410.3012 [hep-ph] (cit. on p. 6).
- [20] C. Degrande et al., *Automated one-loop computations in the Standard Model Effective Field Theory*, Phys. Rev. D **103** (2021) 096024, arXiv: 2008.11743 [hep-ph] (cit. on p. 7).
- [21] F. U. Bernlochner, D. C. Fry, S. B. Menary and E. Persson,

 Cover Your Bases: Asymptotic Distributions of the Profile Likelihood Ratio When Constraining

 Effective Field Theories in High-Energy Physics, 2022, arXiv: 2207.01350 [physics.data-an]

 (cit. on p. 7).